JOURNAL OF THERMOPHYSICS AND HEAT TRANSFER
Vol. 13, No. 4, October–December 1999

Interaction of Spalled Particles with Shock Layer Flow

Chul Park*
NASA Ames Research Center, Moffett Field, California 94035-1000

The influence of the solid particles injected into the shock layer by the spallation of a carbonaceous ablating heatshield on the shock layer flow is investigated theoretically. The equation of motion of a solid particle is integrated using a polynomial expansion. Assuming a Gaussian distribution for the initial masses and velocities of the particles, the rates of production of CO, CN, C_3, and turbulence energy are calculated by integrating those production rates for one particle over the mass and velocity distributions. The results for the environment of Stardust Earth reentry show that these production rates decay approximately exponentially in the normal direction from the ablating wall. Correlation formulas for the magnitudes and slopes of this decay pattern are derived. The lower limits of particle size and initial velocity are estimated for a carbon-phenolic material from a spectroscopic result obtained in an arcjet wind-tunnel test.

Nomenclature

A_i = coefficients in Eq. (11) and Table 2
a = normalized vaporization rate [Eq. (7a)]
C_d = drag coefficient of a particle
C_n = average molecular speed of nitrogen atoms, cm/s
C_o = average molecular speed of oxygen atoms, cm/s
C_s = average molecular speed of C_3 emerging from particle, cm/s
C_t = average molecular speed of flow, cm/s
d_r = characteristic initial particle diameter [Eq. (1b)], cm
G = production rate [Eq. (10)]
k = Boltzmann constant
M = spallation rate at x_0, g/(cm^2-s)
M_0 = spallation rate at stagnation point, g/(cm^2-s)
m_i = mass of one atom/molecule of species i, g
m_r = characteristic initial particle mass [Eqs. (1a) and (1b)], g
m_0 = initial mass of one particle, g
N_n = number density of nitrogen atoms, cm^{-3}
N_o = number density of oxygen atoms, cm^{-3}
N_{se} = number density of equilibrium vapor of C_3, cm^{-3}
N_t = total number density, cm^{-3}
p_s = stagnation pressure, atm
q = production rate for one particle [Eqs. (9a–9f)]
q_c = convective heating rate to particle, erg/(cm^2-s)
q_r = radiative heating rate to particle, erg/(cm^2-s)
q_s = heating rate due to surface reaction, erg/(cm^2-s)
R = radial distance (Fig. 2a), cm
R_b = base radius (Fig. 2a), cm
R_e = Reynolds number
R_n = nose radius (Fig. 2a), cm
r = radius of one particle, cm
T = gas temperature, K
T_w = wall temperature of particle, K
t = time, s
t' = normalized time
U = x component of flow velocity, cm/s
u = x-component of particle velocity, cm/s
u' = normalized u
V = y component of flow velocity, cm/s
V_e = V value behind shock wave, cm/s
V_f = freestream velocity, cm/s
v = y component of particle velocity, cm/s
v_r = characteristic initial velocity, cm/s
v_0 = initial velocity of one particle, cm/s
v' = normalized v
w = $\sqrt{[(U-u)^2+(V-v)^2]}$, cm/s
X = independent variable of correlation [Eq. (11)]
x = distance along wall measured from x_0, cm
x_0 = particle ejection point (Figs. 2a and 2b), cm
x' = x/Δ_0
Y = dependent variable of correlation [Eq. (11)]
y = distance normal to wall, cm
y' = y/Δ_0
z = axial distance (Fig. 2a), cm
α = mass distribution parameter [Eq. (1a)]
β = velocity distribution parameter [Eq. (1c)]
Δ = local shock layer thickness, cm
Δ_0 = shock layer thickness at stagnation point, cm
η_n = nitridation coefficient
η_o = oxidation coefficient
η_s = sublimation coefficient
θ = polar angle (Fig. 2b)
ρ = gas density, g/cm^3
ρ_s = density of particle, g/cm^3
σ = Stefan–Boltzmann constant

Subscripts

e = behind the shock wave
n = nitridation
o = oxidation
s = sublimation

Introduction

Background

FOR some of the planetary entry flights, the heat transfer rates to the heatshield protecting the vehicle are sufficiently high to cause ablation. For the Apollo, Pioneer–Venus, and Galileo vehicles, the heat transfer rate, the temperature rise in the heatshield, or the extents of ablation were measured. When those measured quantitites were compared with theoretical calculations, discrepancies were found.[1–3] For both Pioneer–Venus and Galileo probe vehicles, heating/ablating rates were overpredicted at the stagnation point and underpredicted in the downstream frustum region.

An interplanetary Earth-return mission named Stardust has recently been launched by the United States,[4] and a similar mis-

Presented as Paper 99-0353 at the AIAA 37th Aerospace Sciences Meeting, Reno, NV, 11–14 January 1999; received 19 February 1999; revision received 21 May 1999; accepted for publication 13 June 1999.

*Senior Research Scientist, Mail Stop 229-1, Thermosciences Institute; cpark@mail.arc.nasa.gov. Associate Fellow AIAA.

sion, named Mu-Science-Engineering-Satellite (MUSES)-C, is being prepared by Japan.[5] Additional similar missions are expected. In these missions, a spacecraft is to enter Earth's atmosphere at a velocity of about 12 km/s. To design such a spacecraft more efficiently, it is desirable to develop a method of predicting ablation rates more accurately.

Pioneer–Venus and Galileo data suggest that there are additional mechanisms that increase heat transfer rates in the downstream region. One such possible mechanism is spallation, which is a phenomenon whereby solid particles are ejected from the ablating surface with a finite velocity. By this process, solid particles consisting mostly of carbon enter the inviscid region where the temperature is high. There the particles vaporize and release carbonaceous gas species.[6] Carbonaceous species are known to radiate strongly. Additionally, because the particles are generally moving slower than the gas flow, the flow is disturbed. This disturbance may cause turbulence.

The spalling particles are likely to be produced by two different physical phenomena. First, during the process of pyrolysis, soot may be formed from the pyrolysis gas. Second, the carbon fibers forming the char may fragment and break loose under heating. There are three possible forces that could push these particles outward: The first is the pressure of the pyrolysis gas inside the heatshield. The second is the deceleration of the reentering vehicle, producing a virtual body force in the outward direction in relation to the vehicle. The third force takes place as a particle emerges from the wall, and, according to existing evidence, it is spun by the velocity gradient in the boundary-layer flow. The relative velocity between the flow and the spinning particle produces a Magnus force that is in the outward direction.

Experimental Evidence

In a first such effort,[7] spallation was determined in a laser-heating experiment to account for 13% of the total ablated material. The threshold heating rate for spallation was determined to be above 8.5 kW/cm^2. However, in a later experiment in an arcjet wind tunnel, spallation rate was deduced to be about 6% of the ablation rate at a heating rate of about 7 kW/cm^2 (Ref. 8). The spallation threshold observed in a ballistic range test, which produces deceleration, is even lower. In one experiment, models in the shape of a flat circular disk were flown in a ballistic range. Spallation was observed photographically at a heating rate of only 0.4 kW/cm^2 (Refs. 9 and 10). With models in the shape of a 45 deg sphere–cone that produced heating rates of the order of 20 kW/cm^2, the spallation rate was determined to be about 40% of the ablation rate.[11]

Recently, a spectroscopic observation was made of flow around a carbon-phenolic flat disk, 2.5 cm in radius, ablating in an arc-heated wind tunnel.[12,13] The spectroscopic observation was made from the side-on direction to view along a line of sight parallel to and upstream of the ablating surface. The location of the line of sight is unknown, but is believed to be of the order of 2 cm in front of the ablating surface, which is in the inviscid region. The result, reproduced in Fig. 1 in the form of a microphoto-densitograph, shows that one of the strongest radiation emitters is CN. Spallation is the most likely mechanism by which carbon can reach the distance so far away from the ablating surface.

Approach

In Refs. 6 and 14, trajectories of spalled particles were calculated numerically by integrating the equation of motion of the particles. In Ref. 6, the decrease in the radius of the particles due to vaporization was calculated simultaneously with the equation of motion by integrating a rate equation. By carrying out such calculations for all possible combinations of initial particle size m_0, initial particle velocity v_0, and flow conditions and geometry and evaluating their consequences on radiation and turbulence, one could, in principle, calculate the spallation effects ab initio. However, such a calculation is presently unwarranted because there are too many unknown parameters governing the phenomena. Instead, the following approach is taken in the present work:

1) A fixed set of values is assumed for the parameters for which we know the order of their magnitudes. This includes drag coefficient, shape, and density of solid particles and average values of the dynamic and thermodynamic properties of the flow along the flight path of one particle.

2) The initial mass m_0 and the initial velocity v_0 are assumed to be described by a generalized Gaussian function characterized by the characteristic mass and velocity m_r and v_r, respectively, and the exponents α and β as

$$f_m(m_0)m_0\,\mathrm{d}m_0 = \frac{2\exp[-(m_0/m_r)^2]m_0^{\alpha}\,\mathrm{d}m_0}{m_r^{\alpha+1}\Gamma[(\alpha+1)/2)]} \tag{1a}$$

where

$$m_0 = (\pi/6)d_0^3\rho_s, \qquad m_r = (\pi/6)d_r^3\rho_s \tag{1b}$$

$$f_v(v_0)\,\mathrm{d}v_0 = \frac{2\exp[-(v_0/v_r)^2]v_0^{\beta}\,\mathrm{d}v_0}{v_r^{\beta+1}\Gamma[(\beta+1)/2]} \tag{1c}$$

where $\Gamma(a)$ is a gamma function. The integration of these expressions is unity for all values of m_r, v_r, α, and β. The smallest interger values of α and β giving a zero value and slope at the origin ($v_r = d_r = 0$) $\alpha = \beta = 2$ are adopted. The uncertainty in α and β is inconsequential, as will be shown later in the Discussion section. The spallation rate M is assumed to be describable by

$$M = M_0\cos^2(\theta) \tag{1d}$$

where M_0 is the value at the stagnation point. The integral

$$\int Mf_m f_v\,\mathrm{d}m_0\,\mathrm{d}v_0$$

has a unit of cm^{-2}s^{-1}.

3) The trajectories of particles are calculated over all points on the ablating surface accounting for vaporization for ranges of v_0 and m_0 values satisfying Eqs. (1a) and (1c) and $M_0 = 1$ g/(cm^2-s). From the trajectory results, the quantitites of interest are determined. The quantitites so determined are summed over the ablating surface and integrated over the distributions [Eqs. (1a) and (1c)]. The results are expressed as functions of v_r and d_r. The choice of M_0 is immaterial: All calculated quantities will be proportional to M_0.

4) By comparing with the experimental evidence given in Fig. 1, plausible lower limits on the values of m_r and v_r are determined for the carbon-phenolic material.

Derivation

Trajectory of One Particle

The coordinate system used is shown in Figs. 2a and 2b. The trajectory of a particle is calculated under the following assumptions: 1) The particles consist of pure carbon with a density of 1 g/cm^3. 2) The particles are spherical in shape. 3) The particles emerge from the ablating wall normally. 4) The drag coefficient C_d is unity. 5) The thermodynamic properties are uniform in the y direction. 6) The flow is inviscid. 7) The tangential flow velocity U is constant across the shock layer. 8) The normal flow velocity V is inversely proportional to y.

The inviscid-flow assumption is made because the spallation effect is important only in the inviscid region; in the boundary layer, there is already a substantial concentration of gaseous carbonaceous species and most likely flow is turbulent because of ablation.[15] Therefore, the presence of particles becomes unimportant. The assumption that the particles emerge normally is inconsequential: The emerging velocity can be decomposed into the normal and the tangential components. Because the absolute value of the emerging velocity is much smaller than the flow velocity, the tangential component has little effect on the behavior of the particles.

Three flow geometries are considered, a hemispherical nose, a cone, and a flat disk (shown in Figs. 2a and 2b) because most planetary entry vehicles have a sphere–cone geometry, and arcjet models

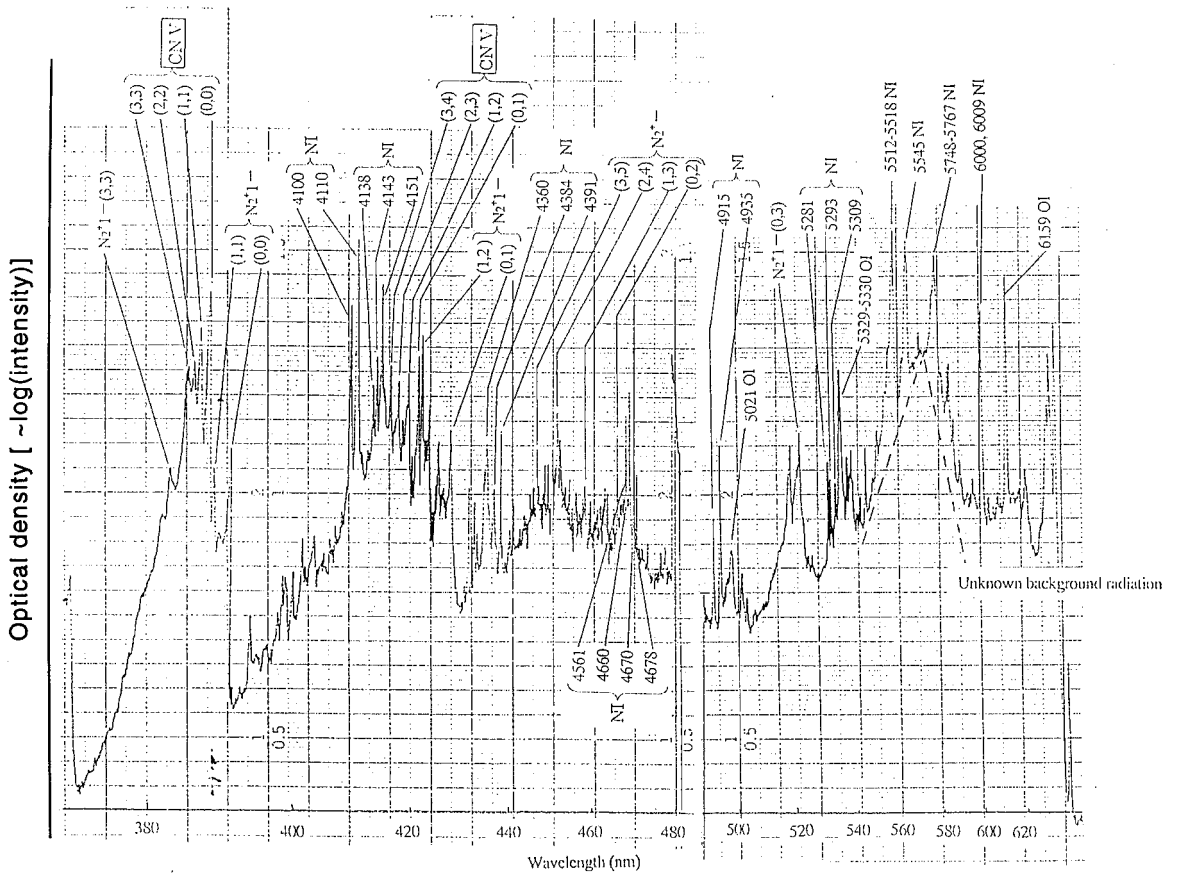

Fig. 1 Microphoto-densitograph of the spectra of radiation from a shock layer over an ablating model taken in an arc-heated wind tunnel.[13]

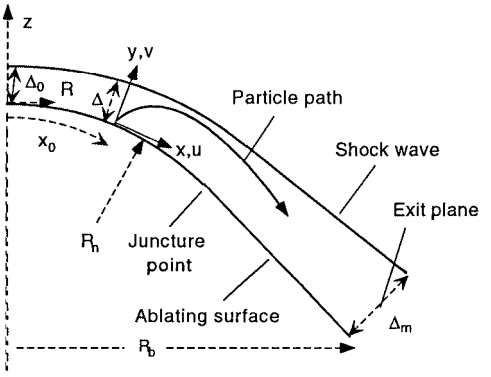

a) Sphere–cone

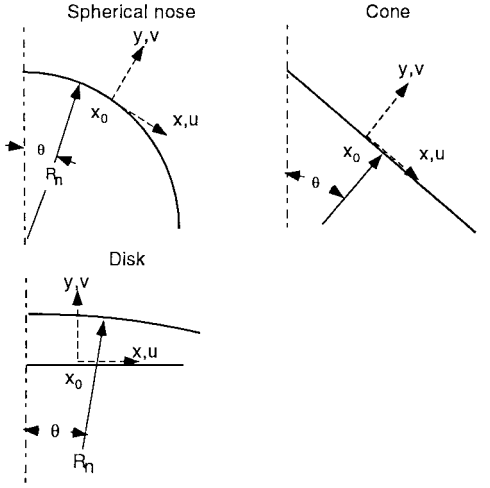

b) Sphere, cone, and disk

Fig. 2 Coordinate system used.

are in the shape of a flat disk. The solution over a sphere–cone is obtained by joining those for a hemisphere and a cone at the juncture.

The expression for the drag force is well known. The equation of motion for a particle around a spherical nose is

$$\frac{du}{dt} = \frac{x}{(R_n + y)^2}\left(u - \frac{x}{R_n + y}v\right) + \frac{1}{m}\left(\frac{x}{R_n + y}f_y + f_x\right) \quad (2a)$$

$$\frac{dv}{dt} = \frac{1}{R_n + y}\left(u - \frac{x}{R_n + y}y\right)^2 + \frac{f_y}{m} \quad (2b)$$

where f_x and f_y are the x and y components of the drag force. For a disk and a cone, they are

$$\frac{du}{dt} = \frac{f_x}{m} \quad (2c)$$

$$\frac{dv}{dt} = \frac{f_y}{m} \quad (2d)$$

The oxidation of carbon surface by atomic oxygen (oxidation)

$$O + C(c) \rightarrow CO + 3.74\,eV \quad (3a)$$

is well known.[16] The spectroscopic result shown in Fig. 1 suggests that a similar process occurs for atomic nitrogen (nitridation):

$$N + C(c) \rightarrow CN + 0.35\,eV \quad (3b)$$

This process will be referred to hereafter as the nitridation process. Sublimation of carbon produces C_n species where n may range from 1 to 5. According to observation,[17,18] however, the most prevalent process (sublimation) is

$$C(c) \rightarrow C_3 - 8.40\,eV \quad (3c)$$

Therefore, only this process is considered.

The coefficient of surface oxidation [Eq. (3a)] is found from experiment as[16] $\eta_o = 0.63\exp(-1160/T_w)$. In a free-molecular flow, the average molecular velocity of the oxygen atoms reaching the particle surface is $C_o = \sqrt{(8kT/\pi m_o)}$. The total rate of arrival of oxygen atoms at the particle surface in the free-molecular regime is expressed as a sum of the molecular arrival rate $N_o C_o/4$, integrated over the global sphere area $4\pi r^2$, and the hypersonic Newtonian value $N_o w$ integrated over the impacting surface area πr^2. This free-molecular value is divided by $\sqrt{(1+Re)}$, where Re is a Reynolds number, to account for the transition to a continuum flow. The Reynolds number is approximated by $Re = \rho(C_o + w)\,\mathrm{d}/\mu$. Viscosity μ is approximated by $\mu = 2\times10^{-4}\sqrt{(T/300)}$ P. By multiplying the arrival rate by η_o, one obtains the rate of removal (g/s) of oxygen atoms:

$$\left(\frac{\mathrm{d}m}{\mathrm{d}t}\right)_o = -\pi r^2 \eta_o N_o (C_o + w) m_o/\sqrt{1+Re} \tag{4a}$$

The coefficient of surface nitridation process [Eq. (3b)] has never been measured. It is assumed tentatively to be the same as that of oxidation, that is, $\eta_n = \eta_o$. The equilibrium vapor number density of C_3 can be written as[17] $N_{se} = 1.15\times10^{27}\exp(-59{,}410/T_w)/T_w$ cm^{-3}. The coefficient of sublimation can be written as[18] $\eta_s = 30\exp(-21{,}490/T_w)$. The rate of mass removal by surface nitridation, $(\mathrm{d}m/\mathrm{d}t)_n$, and by sublimation, $(\mathrm{d}m/\mathrm{d}t)_s$, can be expressed in a similar manner. The rate of change of particle mass (g/s) is determined from these three rates as

$$\frac{\mathrm{d}m}{\mathrm{d}t} = \frac{m_c}{m_o}\left(\frac{\mathrm{d}m}{\mathrm{d}t}\right)_o + \frac{m_c}{m_n}\left(\frac{\mathrm{d}m}{\mathrm{d}t}\right)_n + \left(\frac{\mathrm{d}m}{\mathrm{d}t}\right)_s \tag{4b}$$

To evaluate η_o, η_n, and η_s, one needs to know the surface temperature of the particle, T_w. It is determined from the condition of steady-state energy balance at the particle surface. The surface is heated by the collisions of atoms and molecules, surface oxidation, nitridation, and flow irradiation. It is cooled by sublimation and surface radiation. The convective heating rate [erg/(cm^2-s)] is calculated in a manner similar to that for atomic oxygen removal rate:

$$q_c = (0.25N_t C_t \times 1.5kT + 0.5\rho w^3)/\sqrt{1+Re} \tag{5a}$$

The surface reactions produce heat in an amount [erg/(cm^2-s)]

$$q_s = \left(6.040\times10^{-11}N_o C_o \eta_o + 5.66\times10^{-13}N_n C_n \eta_n - 1.35\times10^{-11}N_{se}C_s\eta_s\right)\Big/\left(1+\sqrt{Re}\right) \tag{5b}$$

where C_s is the average molecular velocity of the C_3 molecules leaving the particle surface. The wall temperature T_w satisfies the equation

$$q_c + q_s + q_r - 1.346\times10^{-11}N_{se}C_w\eta_s - \sigma T_w^4 = 0 \tag{5c}$$

where q_r is the radiative flux incident on the particle. Equation (5c) is solved through a Newton's iterative procedure.

For convenience, x, y, and t are first normalized by

$$x' = (x - x_0)/\Delta_0 \tag{6a}$$

$$y' = y/\Delta_0 \tag{6b}$$

$$t' = (v_0/\Delta_0)t \tag{6c}$$

U is approximated for the hemisphere and the flat disk by $U = (\mathrm{d}U/\mathrm{d}x)x$. The velocity gradient $\mathrm{d}U/\mathrm{d}x$ is approximated in turn by $0.75V_f/R_n$. For the flow over a cone, U is given by $U = V_f\sin(\theta)$. V is approximated by $V = -V_e y/\Delta$ for all three geometries.

The differential equations in Eqs. (2a–2d) are integrated in the form of a series expansion in t. By the assumption that the particles emerge normally from the surface, one has $v = v_0$ and $u = 0$ at $t = 0$. The variables x and y are expressed nondimensionally by

$$x' = a_1 t'^2 + a_2 t'^3 + a_3 t'^4 \tag{6d}$$

$$y' = t' + b_2 t'^2 + b_3 t'^3 + b_4 t'^4 \tag{6e}$$

By expanding both the left- and the right-hand sides of Eqs. (2a–2d) in powers of t' and equating the like terms, the coefficients a' and b' are determined. Trial and error shows that a better agreement with a numerical integration of Eqs. (2a–2d) can be obtained if a_3 and b_4 obtained from this procedure are multiplied by 1.5. This procedure probably partly accounts for the higher-order terms neglected in Eqs. (6d) and (6e).

The parameter that controls the rate of vaporization is

$$a = \frac{\pi}{3}\frac{\Delta}{v_0}\frac{1}{m_0^{\frac{1}{3}}}\left(\frac{3}{4}\frac{1}{\pi\rho_s}\right)^{\frac{2}{3}}[N_o(C_o+w)m_c\eta_o + N_n(C_n+w)m_c\eta_n + N_{se}C_s m_{c3}\eta_s]/\sqrt{1+Re} \tag{7a}$$

If a is constant, Eq. (4c) can be integrated in a closed form:

$$m = m_0(1 - at')^3 \tag{7b}$$

In reality, a is not constant. An approximate constant best-matching value of a was assumed to be in a form

$$a = Aa_b(Ba_a/a_b)^C \tag{8a}$$

where a_a is the a value evaluated at $U = V = u = v = 0$ and a_b is that value evaluated at $U = U_e$, $Re = 0$, $V = u = v = 0$. The constants A, B, and C are determined so as to satisfy the global mass conservation condition, as will be explained in the Calculation Procedure section, for many different values of m_r and v_r. The selected values of A, B, and C lead to

$$a = 0.8a_b(5a_a/a_b)^{1.5} \tag{8b}$$

This average a is used in Eq. (7b).

In Figs. 3a and 3b, comparison is made between the present polynomial approximation and a numerical integration of Eqs. (2a–2d), (4a), and (4b), for typical cases. As seen here, agreement is good within the interested range of x and y, at least for these cases.

For an arbitrarily given starting point x_0 (Figs. 2a and 2b) and a specified downstream location x, one can determine the flight time t' by solving Eq. (6d). By substituting that t' value into Eq. (6e), one can determine the value of y that corresponds to the original x.

Influence on Flow by One Particle

The rate of removal of oxygen atoms per unit length in the x direction is obtained by dividing Eq. (4a) by u(g/cm):

$$q_o = -\frac{\pi r^2 \eta_o N_o (C_o + w) m_o}{u\sqrt{1+Re}} \tag{9a}$$

The process produces CO molecules in return at a rate (g/cm) of

$$q_{co} = -(m_{co}/m_o)q_o \tag{9b}$$

Likewise, nitrogen atoms are removed and CN molecules are formed at the rates (g/cm) of

$$q_n = -\frac{\pi r^2 \eta_n N_n (C_n + w) m_n}{u\sqrt{1+Re}} \tag{9c}$$

$$q_{cn} = -(m_{cn}/m_n)q_3 \tag{9d}$$

Sublimation produces C_3 molecules at the rate (g/cm) of

$$q_{c3} = \frac{\pi r^2 \eta_s N_{se} C_s m_{c3}}{u\sqrt{1+Re}} \tag{9e}$$

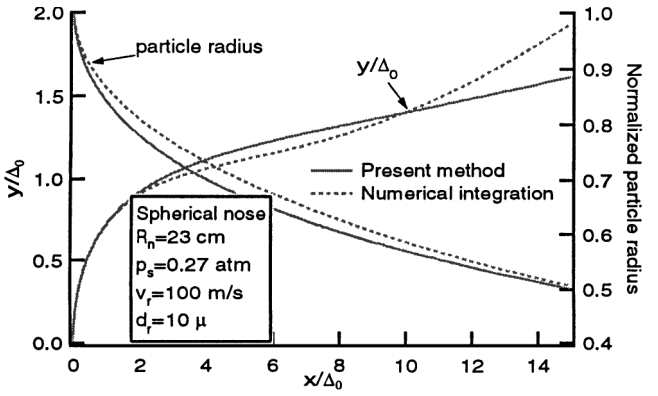

a) Spherical nose, $\Delta_0 = 1$ cm, $x_0/R_n = 0.3$

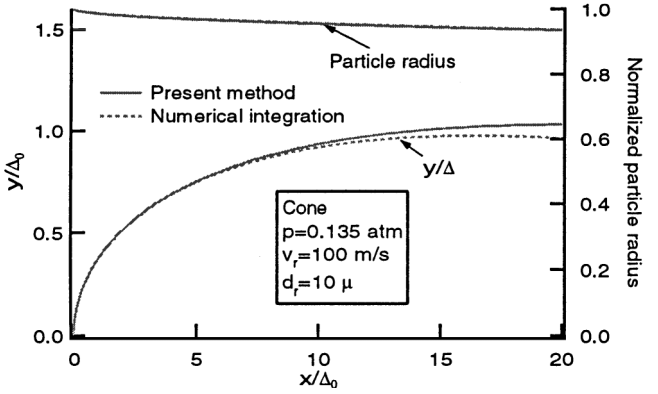

b) Cone, $\theta = 45$ deg, $x_0 = 14.1$ cm

Fig. 3 Particle radius and particle trajectory comparison between present analytical method and numerical integration: $V_f = 12$ km/s, $\rho_f = 1.88 \times 10^{-7}$ g/cm^3.

The kinetic energy of the flow is disturbed by the drag work, oxidation, nitridation, and sublimation. The drag work (erg/cm) deposited within the 1 cm along the streamline is

$$q_{6a} = (C_d/2)\pi r^2 \rho[(U-u)^2 + (V-v)^2]$$

Oxygen and nitrogen atoms are removed by surface oxidation and nitridation, but this occurs without causing any disturbance. However, when the CO, CN, and C_3 molecules emerge as a result of the surface reactions, they appear with a velocity different from the flow velocity. The disturbance energies (erg/cm) caused by this mechanism are

$$q_{6b} = \left\{\pi r^2 N_o C_o \eta_o m_{co}[(U-u)^2 + (V-v)^2]/2w\right\}$$

$$q_{6c} = \left\{\pi r^2 N_n C_n \eta_n m_{cn}[(U-u)^2 + (V-v)^2]/2w\right\}$$

$$q_{6d} = \left\{\pi r^2 N_{se} C_s \eta_s m_{c3}[(U-u)^2 + (V-v)^2]/2w\right\}$$

The ratio of the total turbulence energy produced by one particle to the flow energy per second is (cm^2)

$$q_6 = \frac{q_{6a} + q_{6b} + q_{6c} + q_{6d}}{0.5\rho(U^2 + V^2)} \qquad (9f)$$

Calculation Procedure

At any specified point x and y, the quantitites q [Eqs. (9a–9f)] are multiplied by the ablation rate $M(x_0)$ and summed over the initial location x_0. The summed values are multiplied by $f_m f_v$ and integrated over m_0 and v_0, that is,

$$G = \int\int \left[\Sigma_{x_0} M(x_0) q(x_0, m_0, v_0)\right] f_m f_v \, \mathrm{d}m_0 \, \mathrm{d}v_0 \qquad (10)$$

The quantity G represents the effect of spallation on the flow and is in the form of a rate of production, that is, g/(cm^{3}s) for q_1–q_5 and s^{-1} for q_6. The integrations are performed numerically.

The particle path calculation starts from the stagnation region. The stagnation point itself is singular, and, therefore, the present calculation starts from the next node point. The calculation is carried out up to the sphere–cone juncture point assuming the body to be a sphere. After the juncture point, the body is assumed to be a cone that extends upstream to its apex. The calculation is started from the extreme upstream point of this hypothetical cone to determine the influence of the upstream points on the points downstream of the juncture point.

The calculation ignores the presence of the bow shock wave and assumes that the properties ahead of the shock wave are the same as those behind. This assumption probably produces only a small error because most particles of interest are behind the shock wave.

After obtaining the production rates G at all points in the flowfield, the mass flux of the particles hitting the heatshield wall, the mass flux of particles leaving the computational domain through the exit plane, and the spatial integration of the production rate of elemental carbon in the flowfield are evaluated. The sum of these three fluxes is the global sum of the rate of the disappearance of elemental carbon in the flowfield and must equal the surface integration of the source M if the mass of carbon is to be conserved. A test is made to verify this mass balance. The mass ratio (i.e., the ratio of the surface integration of M to the global sum) is calculated for arbitrarily chosen m_r and v_r values. Initially A, B, and C in Eq. (8a) were varied also. The ratio was found to depend partly on the fineness of the grid. A grid of 51×51 was found to be necessary for a grid-independent solution. With a 51×51 grid, A, B, and C were varied until the mass balance is satisfied for different values of m_r and v_r. The chosen A, B, and C values are given in Eq. (8b).

The deviation from mass conservation at grids smaller than 51×51 may be attributed to 1) the truncation error in the polynomial expressions [Eqs. (6d) and (6e)], 2) the use of an approximation in determining a [Eq. (8b)], 3) the approximations for species production rates [Eqs. (9a–9f)], and 4) the numerical errors in the three layers of integration performed. The calculated G values are multiplied by the mass ratio to produce the final G values that satisfy the mass conservation requirement.

For all cases considered, the radiative heating rate q_r was negligibly small compared with other terms in Eq. (5c), which are of the order of 10^5 W/cm^2. The q_r was kept as 100 W/cm^2, a typical value for Stardust entry environment, throughout. Gas temperature, which enters into consideration in calculating number densities, was assumed to vary as $\cos(\theta)$ between the stagnation and frustum region values. For a mesh of 51×51, the entire calculation requires approximately 2.8 min on an SGI Origin 200 work station.

Results

General Features

The geometry of the sphere–cone geometry chosen is that of Stardust vehicle.[4] The flow environment is given in Table 1. In Figs. 4a and 4b, typical calculated results are shown for the rates of production of CO and turbulence, respectively, in the form of equipotentials. The curves show the points where the calculated rate values equal the indicated fractions of the reference maximum value over frustum. The stagnation pressure of 0.29 atm corresponds to the peak heating point in the entry trajectory.[4] The production rates of CN and C_3 are qualitatively similar to those shown in Fig. 4 and, therefore, are not presented. Numerical values of this solution are presented in Table 1.

Figures 4a and 4b show that the production rates are zero in the stagnation region. This is partly because the stagnation point is a singular point, and calculation is not performed there. However, it is mostly because the particles are pushed downstream. Theoretically, the strength of the species production is infinitesimally weak along the stagnation streamline. The reference maximum value is taken at the frustum instead of stagnation point for this reason.

Table 1 Parameters of the solution shown in Figs. 4a and 4b

Quantity	Value
Inputs	
Freestream density	2.34×10^{-7} g/cm^3
Freestream velocity	1.114×10^6 cm/s
Nose radius	23 cm
Frustum radius	40 cm
Cone angle	60 deg
Stagnation pressure	0.29 atm
O concentration	0.2
N concentration	0.75
Stagnation region temperature	12,000 K
Frustum region temperature	10,000 K
α, β	2
d_r	10^{-3} cm
v_r	10^4 cm/s
M_0	1 g/(cm^2-s)
Outputs	
$\int M\,dA$	4,098 g/s
Gaseous C production rate	3,590 g/s
Flux hitting wall	508 g/s
Flux through exit plane	Negligible
Max production rate over frustum	
CO	0.0613 g/(cm^{3}s)
CN	0.219 g/(cm^{3}s)
C_3	0.520 g/(cm^{3}s)
Turbulence energy fraction	6.08×10^4 s^{-1}
e-folding distance at frustum	
CO	0.802 cm
CN	0.802 cm
C_3	1.28 cm
Turbulence energy fraction	6.23 cm
Particle surface temperature	3,700-4,300 K

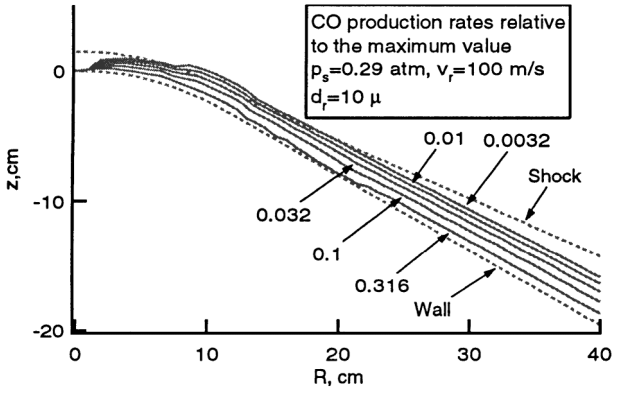

a) CO production rate

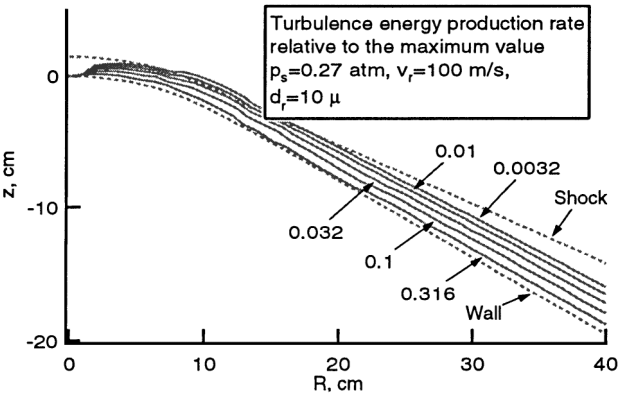

b) Turbulence energy production rate

Fig. 4 Equipotential plot of spallation effects for Stardust case.

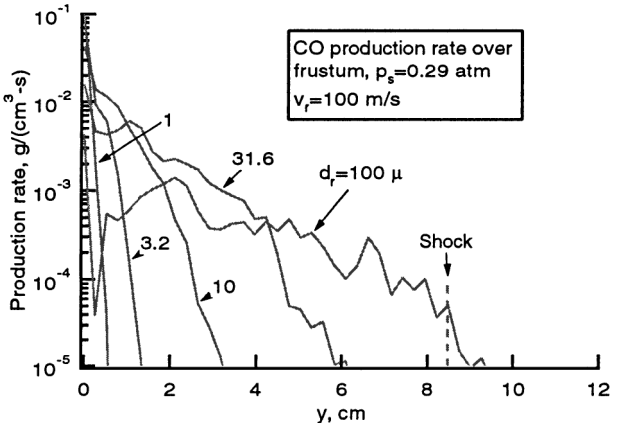

a) As a function of particle size

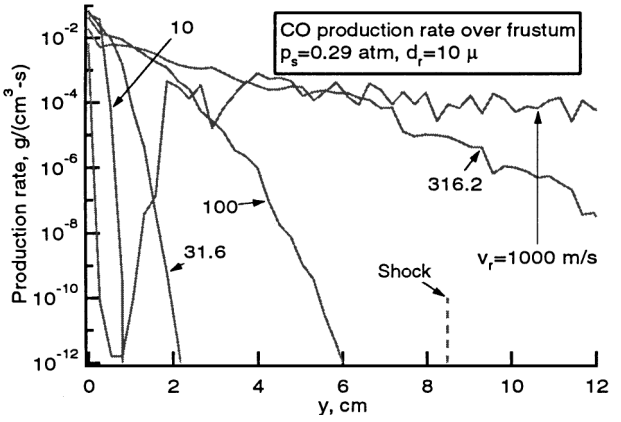

b) As a function of initial velocity

Fig. 5 Distribution of CO production rates across shock layer at frustum: M_0 = 1 g/(cm^2-s).

Calculated quantities are continuous across the sphere-cone juncture, suggesting that the present method of joining the two solutions, one for a spherical nose and the other for a cone, is viable.

The depth of penetration of particles, that is, the distance from the ablating wall to the point where the calculated value falls to a desginated fraction of the reference value, increases toward the downstream in the stagnation region, and remains almost constant over the cone surface.

In Figs. 5a and 5b, the CO production rate is shown across the shock layer over the frustum at different d_r and v_r values. Figure 5 shows a relatively smooth variation of quantities at small y, but a large fluctuation at large y. This is because the number of samples decreases with y. As seen here, larger particles and particles with larger initial velocities penetrate farther into the inviscid shock layer, as expected.

For the largest particle size and largest initial velocity, there is a region near the wall where the calculted rates are low. That is, the particle cloud is detached from the wall. Apparently, the large inertia of these particles causes the particle cloud to exist away from the wall. Except for the detached cases, the calculated quantities decay monotonically away from the wall. Two quantities can be defined: 1) the maximum value, which is at the wall, and 2) the penetration distance defined as the e-folding point, that is, the point where the calculated quantity falls to $1/e$ (36.8%) of the maximum value.

Correlations

The calculation has been repeated over the range of parameters, ρ_f from 2.34×10^{-8} to 7.4×10^{-7} g/cm^3 (corresponding to stagnation pressures from 0.029 to 0.917 atm), v_r from 10^3 to 10^5 cm/s, and d_r from 10^{-4} to 10^{-2} cm, in the steps of a ratio of $\sqrt{10} = 3.162$. From the results, correlation plots were generated. An independent plotting parameter X is defined in the form $X = \ell n(\rho_f^a d_r^b v_r^c)$. Likewise, the dependent plotting parameter Y is defined as $Y = \ell n(G\rho_f^d d_r^e v_r^f)$

Table 2 Correlation formulas

Quantity G	Units	X	Y	Correlation expression
		CO production rate		
Maximum value	g/(cm^3-s)	$\ln\left(\rho_f^{0.5} v_r^{-2.5} d_r^{1.8}\right)$	$\ln\left(GM_0 \rho_f^{-0.7} v_r^{-0.25} d_r^{1.7}\right)$	$Y = 12.54 + 0.2712X + 0.005.648X^2$
e-folding distance	cm	$\ln\left(\rho_f^{-1.8} v_r^{3.3} d_r^{0.6}\right)$	$\ln\left(GM_0 \rho_f^{2.1} v_r^{-3.3} d_r^{-1}\right)$	$Y = -9.328 - 0.8501X + 9.407 \times 10^{-5} X^2$
		CN production rate		
Maximum value	g/(cm^3-s)	$\ln\left(\rho_f^{0.3} v_r^{-2.2} d_r^{2}\right)$	$\ln\left(GM_0 \rho_f^{-0.75} v_r^{-0.4} d_r^{2.1}\right)$	$Y = 15.10\text{E} + 0.3332X + 0.006526X^2$
e-folding distance	cm	$\ln\left(\rho_f^{-1.7} v_r^{3.1} d_r^{0.6}\right)$	$\ln\left(GM_0 \rho_f^{2.2} v_r^{-3.3} d_r^{-1}\right)$	$Y = -10.37 - 0.9182X + 2.513 \times 10^{-4} X^2$
		C_3 production rate		
Maximum value	g/(cm^3-s)	$\ln\left(\rho_f^{0.5} v_r^{-3} d_r\right)$	$\ln\left(GM_0 \rho_f^{-0.8} v_r^{-1} d_r^{1.5}\right)$	$Y = 13.47 + 0.8921X - 0.002657X^2$
e-folding distance	cm^3	$\ln\left(\rho_f^{-0.1} v_r^{0.25} d_r^{0.4}\right)$	$\ln\left(GM_0 \rho_f^{1.4} v_r^{-2.4} d_r^{-3.4}\right)$	$Y = -6.455 - 9.546X + 0.3237X^2$
		Turbulence energy production rate (as fraction of flow kinetic energy)		
Maximum value	s^{-1}	$\ln\left(\rho_f^{-2} v_r^{2} d_r^{-0.7}\right)$	$\ln\left(GM_0 \rho_f^{1.4} v_r^{-0.8} d_r^{1.4}\right)$	$Y = 16.26 - 0.7152 - 0.006699X^2$
e-folding distance	cm	$\ln\left(\rho_f^{-0.1} v_r^{0.2} d_r^{0.35}\right)$	$\ln\left(GM_0 \rho_f^{1.3} v_r^{-1.85} d_r^{-2.95}\right)$	$Y = 2.392 - 15.88X + 1.527X^2$

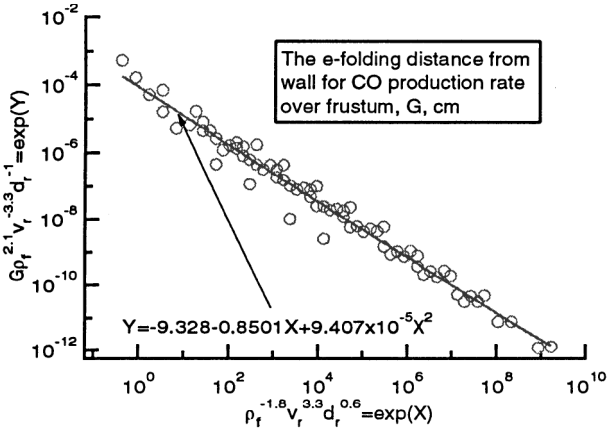

a) CO production rate

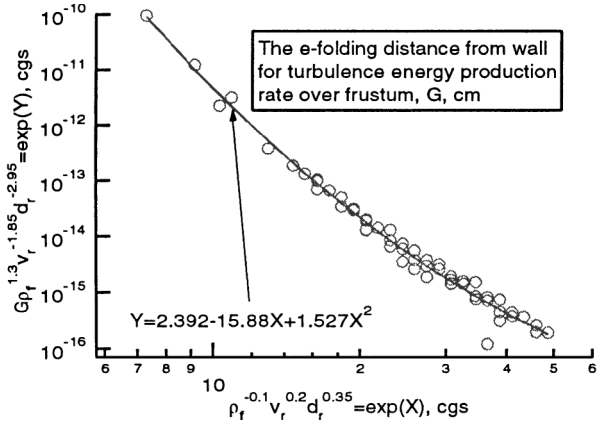

b) Turbulence energy production rate

Fig. 6 Normalized penetration distance: $M_0 = 1$ g/(cm^2-s).

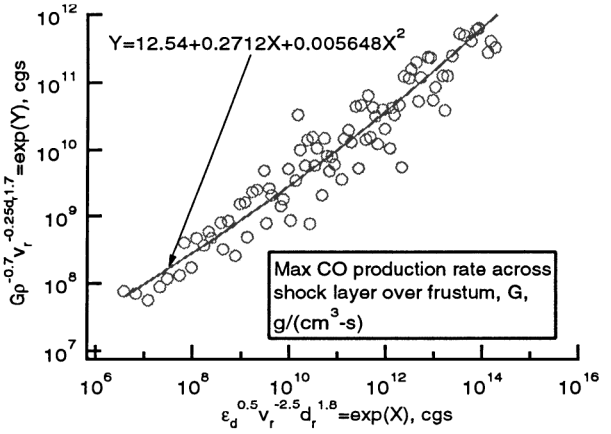

a) CO production rate

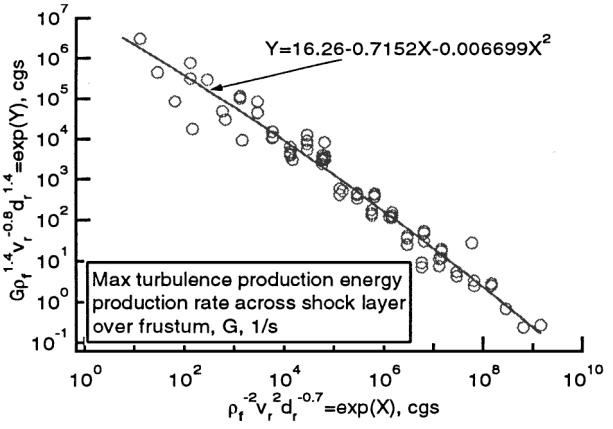

b) Turbulence energy production rate

Fig. 7 Normalized maximum rates: $M_0 = 1$ g/(cm^2-s).

where G is given by Eq. (10). The values of the indices a–f are chosen to produce the smallest standard deviation in the plot. A second-order curve

$$Y = A_0 + A_1 X + A_2 X^2 \tag{11}$$

that best fits the plotted points was found through a least-square curve fit.

In Figs. 6a, 6b, 7a, and 7b, such correlation plots are shown. In Figs. 6a and 6b, the penetration distances at the frustum are shown as G. Only the CO and turbulence energy production rates are shown because the remaining two quantities behave qualitatively the same as those for CO. Figures 7a and 7b show the maximum values, that is, the largest value across the shock layer over the frustum. The correlation parameters are presented for all calculated quantities in Table 2.

Wind-Tunnel Experiment

Calculations are also carried out for the conditions of the spectroscopic experiment mentioned in the Introduction.[12,13] The test flow was subsonic and had a velocity of about 1000 m/s ahead of the body.[19] From the known pressure and a condition that V_e is 1000 m/s at a point 1 cm ahead of the ablating surface, an equivalent

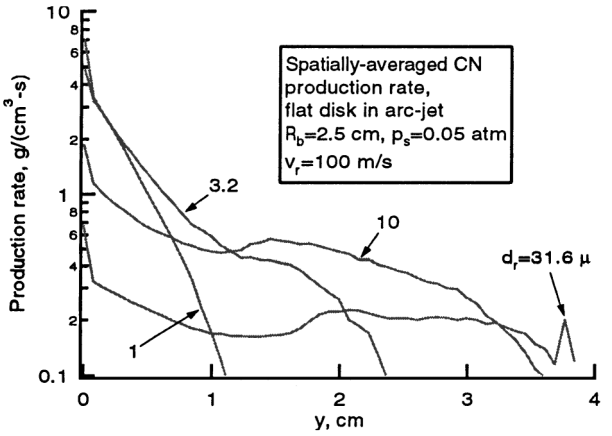

a) As a function of particle diameter

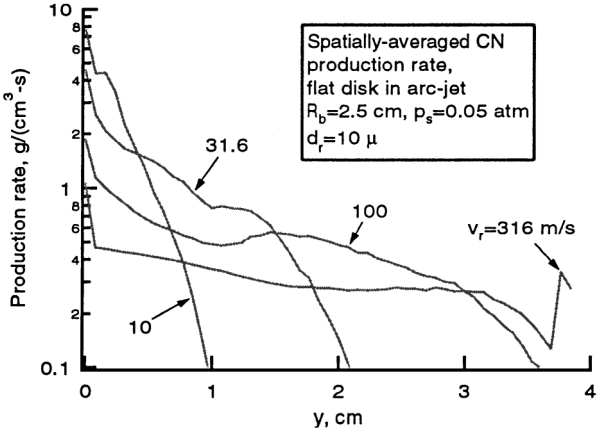

b) As a function of particle initial velocity

Fig. 8 Distribution of CN production rate for a wind-tunnel experiment condition.[13]

hypersonic flow giving the same pressure, the same enthalpy, and the same velocity distribution in the shock layer was determined to be $V_f = 5$ km/s, $\rho_f = 2 \times 10^{-7}$ g/cm^3, and $R_n = 6$ cm. The invisicd flow is assumed to be dissociated to the same extent as is indicated in Table 1. From the calculated distribution of production rate of CN, a spatial integration was performed on the rate of production of CN in the direction parallel to the ablating disk surface. This averaging was carried out because the spectroscopic observation was made in that direction. M_0 was kept as 1 g/(cm^2-s).

The results of these calculations are shown in Figs. 8a and 8b. As mentioned in the Introduction, significant CN radiation was observed at a distance about 2 cm ahead of the disk surface. Because it requires a finite time for the CN molecules produced at the particle surface to be electronically excited and emit radiation, the experiment implies that there was significant production of CN at a distance larger than 2 cm. According to Figs. 8a and 8b, that will happen if either v_r is equal to or greater than 32 m/s when d_r is 10 μ or d_r is equal to or greater than 3.2 μ when v_r is 100 m/s. It is safe to say that v_r and d_r are in the orders of 100 m/s and 10 μ, respectively, for this material.

Discussion

The scatter of the computed points around the correlation curves [Eq. (11)] is relatively small in Figs. 6a and 6b, signifying that the penetration distances may be expressed by Eq. (11) reasonably well. However, the scatter in Figs. 7a and 7b is large, especially in Fig. 7a. This means that the absolute values of the production rates of CO, CN, and C_3 cannot be expressed reliably by Eq. (11). As mentioned in the Calculation Procedure section, the mass flux of spalled carbon, $\int M \, dA$, must equal the spatial integration of the production rates of gaseous carbon (CO, CN, and C_3). When Eq. (11) is used in approximating the distribution of the production rates, the calculated production rates must be corrected by multiplying by the mass ratio mentioned earlier (i.e., the ratio between the surface integration of spallation rate and the global production rate of elmental carbon) to enforce mass conservation.

The absolute values of the maximum species production rate shown in Table 1 are in the range from 0.06 to 0.5 g/(cm^{3}s) for the M_0 value of 1 g/(cm^2-s) considered. Results scale directly with M_0; therefore, if M_0 is 10% of the ablation rate, based on the solution given in Ref. 4, M_0 will be up to 10^{-3} g/(cm^2-s). Therefore, maximum species production rate over the frustum for Stardust vehicle will be between 6×10^{-5} (for CO) and 5×10^{-4} (for C_3) g/(cm^{3}s). The maximum flow residence time in the shock layer is 10^{-4} s. Within that time, CO and C_3 could be produced in concentrations of up to 6×10^{-9} and 5×10^{-8} g/cm^3, respectively, which corresponds to mole fractions of 7.6×10^{-4} and 4.9×10^{-3}, respectively, if the spallation rate is 10% of the ablation rate. C_3 will no doubt decompose and, in the process, may produce more CO and CN. Ultimately, all of these species dissociate into atomic carbon, oxygen, and nitrogen. CO, CN, and atomic carbon are all known to radiate strongly. The concentrations of these species are sufficiently high to increase radiative heat flux to the wall significantly.

Turbulence energy production rate is expressed as a fraction of the flow kinetic energy. Its maximum value is 6×10^4/s for $M_0 =$ 1 g/(cm^2-s). For an M_0 value of 10^{-3} g/(cm^2-s), turbulence intensity may reach up to 0.6% of flow energy within the residence time of 10^{-4} s.

Calculations were carried out with α and β values between 2 and 5. The results show that the larger these values are, the farther into the shock layer the particles penetrate. Larger values of α and β cause the magnitude of the distribution functions [Eqs. (1a) and (1c)] to increase. For the same peak value, the behavior is similar. Thus, larger α and β values are equivalent to larger d_r and v_r. Therefore, the uncertainty in α and β values can be thought to be included in the uncertainty for d_r and v_r.

The characteristic initial velocity v_r was considered to be uniform over the entire ablating surface. As mentioned in the Introduction, v_r is produced partly by the Magnus force generated by the velocity gradient in the boundary layer. This implies that v_r is likely to be small in the stagnation region where the flow velocity is small and large in the downstream region where flow velocity is large. This point should be considered in the application of the present results.

Theoretically evaluating the impact of the spallation phenomena on heat transfer will be a task of considerable complexity. If the flow is assumed to be in equilibrium, the carbonaceous molecules produced, CN, CO, and C_3, are taken to be instantly dissociated and ionized to produce C and C^+ because the temperature is over 10,000 K in the inviscid region. In reality, a finite time is needed for the molecules to be dissociated, and they will exist in the hot environment while the dissociation reaction is in progress. The spectrogram in Fig. 1 is a proof of this. The CN and CO molecules electronically excited by the hot electrons will emit strongly and produce the observed spectra. Calculations made in Ref. 5 demonstrate this point. Therein, for a simple hypothetical uniform slab, two different temperatures are assumed, one for equilibrium and one for nonequilibrium, the nonequilibrium temperature being higher. It is shown that radiative heating rate increases by a factor of 5 or 35 by addition of 2% by mass of carbon depending on whether the flow is in equilibrium or nonequilibrium. For these reasons, it is difficult to determine at this time which case gives the higher heating rates: equilibrium or nonequilibrium. To calculate the phenomenon accurately, one needs to carry out nonequilibrium flow calculation including the spallation effects.

By repeating and expanding the spectroscopic measurement shown in Fig. 1 and comparing the results with such nonequilibrium calculations, it should be possible to determine d_r and m_r. The absolute intensity of CN radiation should yield the ablation rate M. Such a task is left for the future.

Conclusions

The rates of production of CO, CN, C_3, and turbulence energy by the drag work and vaporization of the spalled carbon particles

in the inviscid region of a shock layer are calculated from assumed characteristic particle sizes, initial velocities, and rates of spallation. The production rates are zero in the stagnation region, are nearly invariant in the downstream region, and decay roughly exponentially in the normal direction. The maximum values and the slopes of decay of these rates are expressed in terms of the characteristic particle size and velocity and ambient atmospheric density. The spectra of the radiation from the shock layer over a carbon-phenolic model ablating in an arcjet wind tunnel flow suggest that the characteristic diameter and initial velocity of the particles are of the order of 10 μ and 100 m/s, respectively.

Acknowledgment

The author wishes to acknowledge the support provided by NASA Ames Research Center through Contract NAS2-14031 to Eloret.

References

[1]Park, C., "Radiation Enhancement by Nonequilibrium in Earth's Atmosphere," *Journal of Spacecraft and Rockets*, Vol. 22, No. 1, 1985, pp. 27–36.

[2]Wakefield, R. M., and Pitts, W. C., "Analysis of the Heat-Shield Experiment on the Pioneer–Venus Entry Probes," AIAA Paper 80-1494, July 1980.

[3]Milos, F. S., "Galileo Probe Heat Shield Ablation Experiment," *Journal of Spacecraft and Rockets*, Vol. 34, No. 6, 1997, pp. 705–713.

[4]Olynick, D., Chen, Y. K., and Tauber, M. E., "Forebody TPS Sizing with Radiation and Ablation for the Stardust Sample Return Capsule," AIAA Paper 97-2474, June 1997.

[5]Park, C., Abe, T., and Inatani, Y., "Research on the Heatshield for MUSES-C Earth Reentry," AIAA Paper 98-2852, Jan. 1998.

[6]Davies, C. B., and Park, C., "Trajectories of Solid Particles Spalled from a Carbonaceous Heat Shield," *Entry Vehicle Heating and Thermal Protection Systems: Space Shuttle, Solar Starprobe, Jupiter Galileo Probe*, edited by P. E. Bauer and H. E. Collicott, Vol. 85, Progress in Astronautics and Aeronautics, AIAA, New York, 1983, pp. 472–495.

[7]Lundell, J. H., and Dickey, R. R., "Response of Heat-Shield Materials to Intense Laser Radiation," AIAA Paper 78-0138, Jan. 1978.

[8]Park, C., Lundell, J. H., Green, M. J., Winovich, W., and Covington, M. A., "Ablation of Carbonaceous Materials in Hydrogen-Helium Arc-Jet Flow," *AIAA Journal*, Vol. 22, No. 10, 1984, pp. 1491–1498.

[9]Park, C., "Stagnation-Point Ablation of Carbonaceous Flat Disks—Part 1: Theory," *AIAA Journal*, Vol. 21, No. 11, 1983, pp. 1588–1594.

[10]Park, C., "Stagnation-Point Ablation of Carbonaceous Flat Disks—Part 2: Experiment," *AIAA Journal*, Vol. 21, No. 12, 1983, pp. 1748–1754.

[11]Park. C., and Balakrishnan, A., "Ablation of Galileo Probe Heat-Shield Models in a Ballistic Range," *AIAA Journal*, Vol. 23, No. 2, 1985, pp. 301–308.

[12]Laux, T., Auweter-Kurtz, M., Wegmann, T., Morino, Y., Yoshinaka, T., Park, C., and Speckmann, H. D., "Comparison of Ablation Material Tests in a Plasma Wind Tunnel and Laser Heating Facilities," 3rd European Workshop on Thermal Protection Systems, Noordwijk, The Netherlands, March 1998.

[13]Yoshinaka, T., "Spallation Measurement at the Ablator Plasma Wind Tunnel Tests," National Space Development Agency of Japan, NASDA-TMR-970006E, Tokyo, Feb. 1998.

[14]Naughton, J. W., Venkatapathy, E., and Loomis, M. P., "Particle Impact Risk Assessment for Ablative Thermal Protection System," AIAA Paper 98-0166, Jan. 1998.

[15]Park, C., "Injection-Induced Turbulence in Stagnation Point Boundary Layers," *AIAA Journal*, Vol. 22, No. 2, 1984, pp. 219–225.

[16]Park, C., *Nonequilibrium Hypersonic Aerothermodynamics*, Wiley, New York, 1990, p. 351.

[17]Baker, R. L., and Covington, M. A., "The High Temperature Thermochemical Properties of Carbon," NASA TM-84710, March 1992.

[18]Baker, R. L., McDonaugh, J. M., Herr, K. C., Klingberg, R. A., Coffer, J. C., and Covington, M. A., "Carbon Vaporization Condensation Effects," NASA TM-874300, July 1984.

[19]Habiger, H. A., and Auweter-Kurtz, M., "Investigation of an High Enthalpy Air Plasma Flow with Electrostatic Probes," AIAA Paper 96-1864, June 1996.